

# We are IntechOpen, the world's leading publisher of Open Access books Built by scientists, for scientists

6,900

Open access books available

186,000

International authors and editors

200M

Downloads

Our authors are among the

154

Countries delivered to

TOP 1%

most cited scientists

12.2%

Contributors from top 500 universities



WEB OF SCIENCE™

Selection of our books indexed in the Book Citation Index  
in Web of Science™ Core Collection (BKCI)

Interested in publishing with us?  
Contact [book.department@intechopen.com](mailto:book.department@intechopen.com)

Numbers displayed above are based on latest data collected.  
For more information visit [www.intechopen.com](http://www.intechopen.com)



## Chapter

# The Effect of Geometrical Factors on the Surface Pressure Distribution on a Human Phantom Model Following Shock Exposure: A Computational and Experimental Study

*Maciej Skotak, Molly T. Townsend, Eren Alay  
and Namas Chandra*

## Abstract

Experimental data and finite element simulations of an anthropometric surrogate headform was used to evaluate the effect of specimen location and orientation on surface pressures following shock exposures of varying intensity. It was found that surface pressure distributions changed with local flow field disturbances, making it necessary to use data reduction strategies to facilitate comparisons between test locations, shock wave intensities and headform orientations. Non-dimensional parameters, termed amplification factors, were developed to permit direct comparisons of pressure waveform characteristics between incident shock waves differing in intensity, irrespective of headform location and orientation. This approach proved to be a sensitive metric, highlighting the flow field disturbances which exist in different locations and indicating how geometric factors strongly influence the flow field and surface pressure distribution.

**Keywords:** shock wave, shock tube, pressure measurements, human phantom, end effect, numerical simulations, impulse effect, dynamic pressure

## 1. Introduction

The shock tube is a convenient way to generate the shock waves in a controlled fashion, and it has been employed in various research areas for more than a century [1–6]. The design of a compressed gas driven shock tube includes three standard components: driver (breech) and driven sections with an optional end wave eliminator [7, 8]. The differences in the dimensions (volume of the breech, breech-to-test section diameter ratio, length of the driven section) and operation of the tube (type of driven gas, mechanism of driver gas release) have significant impact on the resulting pressure history measured inside of the tube [9]. The classical design of

the shock tube employs the plastic or metal membranes, which is used to confine the driver gas from entering the driven test section. The driver section pressure is gradually increased until the point of mechanical failure of the membrane upon which the driver gas is entering the test section, pressurizing the ambient gas and resulting in the formation of the shock wave. Alternative designs employ membraneless drivers where the piston [10–13], or fast acting valve [14–16], are used eliminating the need for membrane replacement between consecutive tests. Both designs have been demonstrated to allow generation of shock waves with diverse magnitudes and characteristics. It is worth mentioning various instrumental factors, discussed in detail in our recent contribution [17], can affect the quality of recorded pressure waveforms and impact the interpretation of the experimental data.

In the biomedical field, research utilizing shock tubes to investigate mechanisms of blast TBI (bTBI) was invigorated only 20 years ago [18, 19]. The primary goal in this area of research is to replicate conditions associated with field explosions, particularly the primary blast injuries caused exclusively by the interaction of a shock wave with the brain are of interest [20]. Simulation of explosive blast implies that a shock wave closely resembling the Friedlander waveform should be produced and it has become a standard in contemporary bTBI models [7, 21]. Two experimental parameters of paramount importance are the specimen restraint and the location of the test section, where the specimen is exposed to a shock wave. For the inanimate specimen the method of restraint is usually not an issue, however, human phantom models are frequently mounted on a biofidelic neck, e.g., Hybrid III, and when subjected to a shock wave loading rapid acceleration can result in the specimen displacement affecting the pressure loading on the surface. When the animal models are used the head restraint becomes extremely important, particularly for rodents with relatively small body dimensions and low weight. If the proper head restraint measures are not included in the experimental design, it might result in the development of erroneous injury modalities. It's been demonstrated that head acceleration might lead to the development of tertiary blast injuries, which have different injury characteristics than those resulting from shock wave loading [22, 23]. The importance of the test location in the shock tube was a subject of the experimental evaluation in the past by our group [24–26]. These results illustrate significant differences between testing the specimen inside of the shock tube, i.e., at the distance from the exit enough to eliminate influence of any end-effects, versus at the end and outside. Testing outside is undoubtedly more convenient, but carries a number of unwanted drawbacks: (1) the shock wave profile is eroded and typically only short duration waveforms are achievable, (2) there is large dynamic pressure component which might contribute to a variety of errors [27], (3) the loading of the specimen strongly depends on the location with respect to the shock tube exit and diameter due to highly heterogeneous conditions [28, 29]. Testing inside provides much higher level of control over the shock wave profile with the dynamic components resembling these encountered in the field explosions.

Numerical simulations are invaluable tools for mechanistic investigation of short lived phenomena like shock wave interaction with complex biological structures. The numerical models in bTBI research area provide insight into: (1) the transmission and propagation of the blast waves in the brain [8, 30, 31], and (2) mitigation of blast effects by helmets [32–40] or other PPE designed to safeguard the craniofacial area [36]. However, the accuracy of the numerical simulations relies on the validation using high-quality experimental data, e.g., the pressure measured on the surface of the helmet or phantom [8, 35, 39], or intracranial pressure [31, 40]. A related branch of experimental work which is yet to be explored to its full potential for numerical model validation is the use of post-mortem human specimens (PMHSs)

[37, 41, 42], instrumented with surface and intracranial pressure sensors. Existing studies in this area are rare and hindered by the experimental difficulties, not to mention complete impracticalities for the evaluation of PPE performance. It only leaves the use of anthropometric phantoms as the only alternative, which, made of non-biological materials, replicate the geometry to a high degree [8, 31, 39, 43, 44].

In this contribution we performed a comprehensive experimental characterization of the human phantom model instrumented with 10 pressure sensors to measure the response to a shock wave loading. The specimen was tested using large cross-sectional area shock tube using three locations with characterized by divergent flow characteristics. The loading of the specimen was administered via a single shock wave with three nominal intensities (70, 140 and 210 kPa), and surface pressure was probed in three headform orientations with respect to the incident shock wave, i.e., 0, 90 and 180°.

## 2. Methods

### 2.1 The shock tube

The 7 m long square (0.71 × 0.71 m) cross section shock tube was used in all experiments. This device was previously characterized in detail [24, 26]. The driver gas was compressed helium (ultra-high purity, 99.99%, Airgas, Oakland, NJ), which was allowed to flow into the breech separated from the driven section of the shock tube with membranes made of Mylar (Grafix, Cleveland, OH). Upon the rupture of membranes, the driver gas enters the driven section and compresses the ambient air, which in turn generates a shock wave. Three discrete Friedlander waveform shock waves with nominal intensities of approximately 70, 140 and 210 kPa peak overpressure in the test section (T5 sensor, **Figure 1**) were used. All tests were performed at ambient conditions.

### 2.2 Pressure measurement, headform preparation, and instrumentation

The temporal evolution of the incident shock wave waveforms was recorded using seven high frequency response pressure sensors model 134A24 (PCB Piezotronics, Inc., Depew, NY, USA), distributed along the shock tube (**Figure 1**). The pencil probe model ICP<sup>®</sup> 137B24B (PCB Piezotronics Inc., Depew, NY, USA) was used to measure the incident pressure on the outside (PP location, **Figure 1**).

The phantom headform [45], was instrumented with 10 PCB Piezotronics model 102B06 pressure sensors as illustrated in **Figure 2A**. Five medial sensors are located along midline anterior–posterior (H1–H5), and five circumferential sensors: two on the right parietal side (H6 and H7), two in eye sockets (H8 and H9, **Figure 2A**) and one on the left parietal side (H10). These sensors were mounted flush to the surface using tapped holes. The headform was mounted on the Hybrid III neck (Humanetics, Plymouth, MI) [46], in a rigid configuration to eliminate the motion of the headform during shock wave impact. The FOCUS headform-Hybrid III neck the assembly was attached to the adapter plate and bolted to the bottom of the shock tube in the test section in three different locations (**Figure 1**).

A custom LabView program was used to record the pressure waveforms. The data acquisition system is based on PXIe-1082 PCI Express chassis and PXI-6133 S Series multifunction DAQ modules (National Instruments, Austin, TX, USA). The signal of pressure sensors was filtered using 8-channel signal conditioners model 483C05 (PCB Piezotronics Inc., Depew, NY, USA). The pressure waveforms were recorded at 1.0 MHz sampling frequency with an acquisition time of 50 ms.

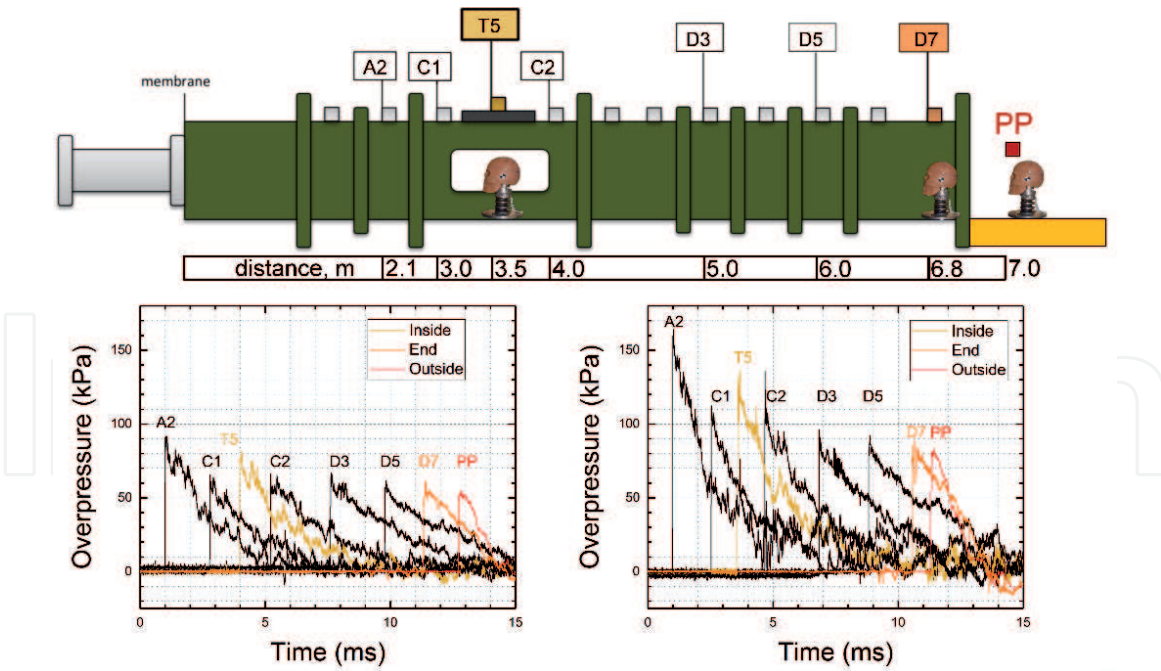


**Figure 1.** Evolution of the shock wave profile traveling in the 28-inch square cross section shock tube. Top panel: schematics of the pressure sensor distribution along the shock tube. The headform is placed in three locations marked as: T5 (inside), D7 (end) and PP (outside). Bottom panels: Pressure profiles of the incident shock wave with nominal BOP of 70 kPa (left) and 140 kPa (right) recorded by sensors distributed along the shock tube as schematically depicted by the top diagram. The shock wave profiles recorded at T5, D7 and PP were used for experimental data normalization. This image was taken from reference [26] (distributed under creative commons attribution (CC BY) license).

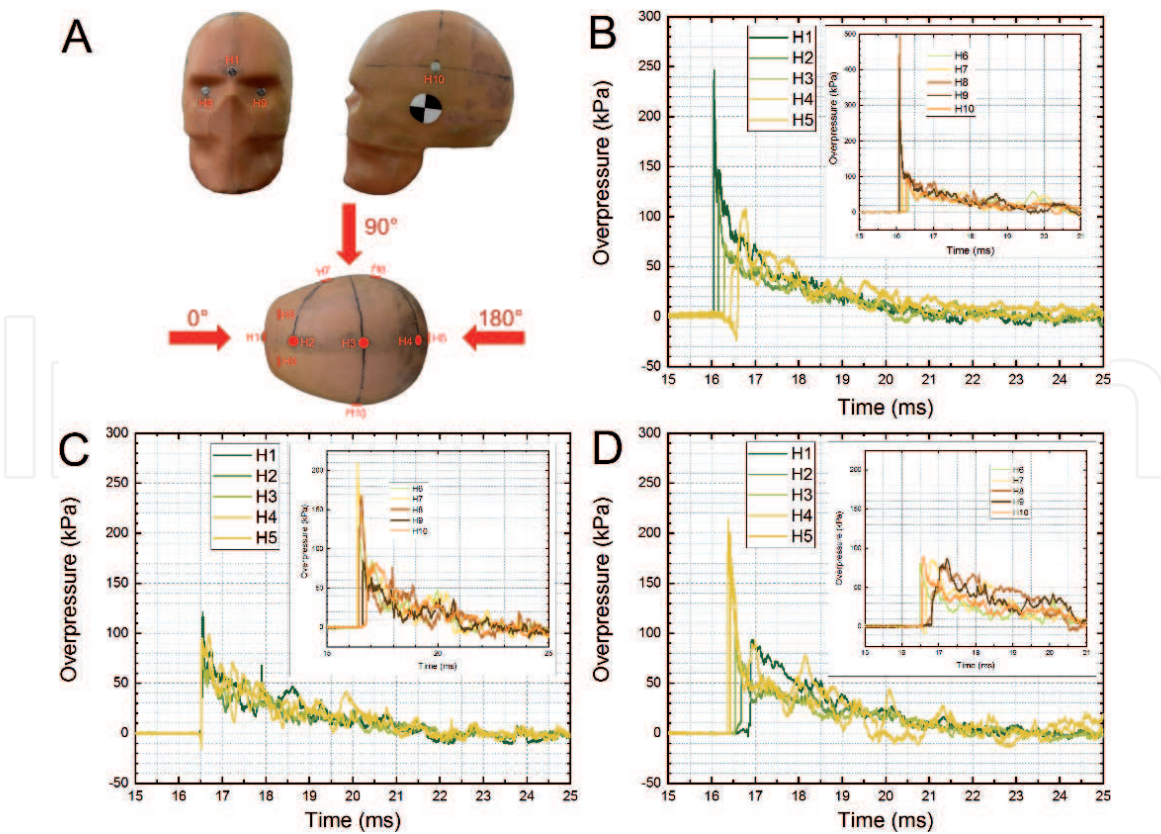


**Figure 2.** The schematic representation of the pressure sensor distribution on the headform (A). The direction of the shock wave propagation in experiments where the headform was rotated in 90° intervals is illustrated. The experimental pressure waveforms collected at 70 kPa nominal shock wave intensity by the surface sensors to three headform orientations: (B) 0°, (C) 90°, and (D) 180° with respect to the direction of the shock wave propagation.

### 2.3 Experimental design, data reduction and statistical analysis

The study was designed as three-factor experimental design,  $3 \times 3 \times 3$ . The three experimental variables investigated are: (1) the headform location (three levels: inside, end and outside, **Figure 1**), (2) the headform orientation (three levels: 0, 90, and 180°), and (3) shock wave intensity (three levels: 70, 140 and 210 kPa).

All pressure waveforms were processed and quantified in Origin 2018 software (OriginLab Corp., Northampton, MA). All data are presented as mean and standard deviation ( $n = 4$ ).

The data normalization and reduction were performed as follows. The four pressure waveform characteristics were tabulated. These include (1) the peak overpressure, the increase in pressure observed at arrival of the shock front, (2) the rise time, or the time required for the pressure to increase from 10 to 90% of the peak overpressure, (3) the positive phase duration, or the time required to return to ambient pressure, and (4) the impulse, or the area under the pressure–time curve during the positive phase duration. Each pressure waveform characteristic value was divided by the incident shock wave equivalent (Eq. (1)):

$$x_{\text{non}} = \frac{x_p}{x_i} \quad (1)$$

where,  $x_p$ —peak overpressure, rise time, duration or impulse of the resulting pressure waveform on the headform,  $x_i$ —peak overpressure, rise time, duration or impulse of the incident shock wave, at the headform location (T5, D7 or PP, **Figure 1**). As a result, a set of normalized non-dimensional peak overpressure, rise time, duration and impulse values is generated for each test location, headform orientation and shock wave intensity.

### 2.4 Flow-field simulations

Finite element models were used to identify the influence the three experimental variables on the flow-field around the specimen. The flow-field around the headform was simulated using a coupled Eulerian-Lagrangian approach to fluid-structure interaction. This solution technique is ideal for the simulation of large deformation finite element analyses and has been used extensively in the simulation of shock-structure interaction physics [8, 47, 48]. The shock wave is modeled in a Eulerian mesh of air and interacts with the headform, modeled using a Lagrangian mesh. The interaction of the two domains results in a solution which depicts the air flow around the headform.

The headform Lagrangian model was generated from a 3D geometrical model generated from the FOCUS headform and the Hybrid III neck using Autodesk Recap Pro 2018 (Autodesk, Inc.). The three-dimensional geometry was meshed using linear tetrahedrons (Simpleware, Synopsys) at a converged mesh density with an average minimum edge length of 8.73 mm (**Figure 3A**). The headform was assumed to be a linear elastic material with a density of 2700 kg/m<sup>3</sup>, an elastic modulus of 6.89 GPa, and a Poisson's ratio of 0.33.

A pre-existing, validated model of a shock tube was enhanced for use as the Eulerian domain [49]. This model used a biased linear hexahedral mesh which converged at a minimum edge length of 14 mm at the region of interest. Two shock tube meshes were used, designed to best model the inside specimen placement and to model the exit and outside specimen placements. The model used to simulate the inside of the shock tube was 5.9 m in length and over 580 thousand elements (**Figure 3B**). The model used to simulate the end and outside specimen placements was 2.9 m in length and over 2.24 million elements (**Figure 3C**). The Eulerian mesh

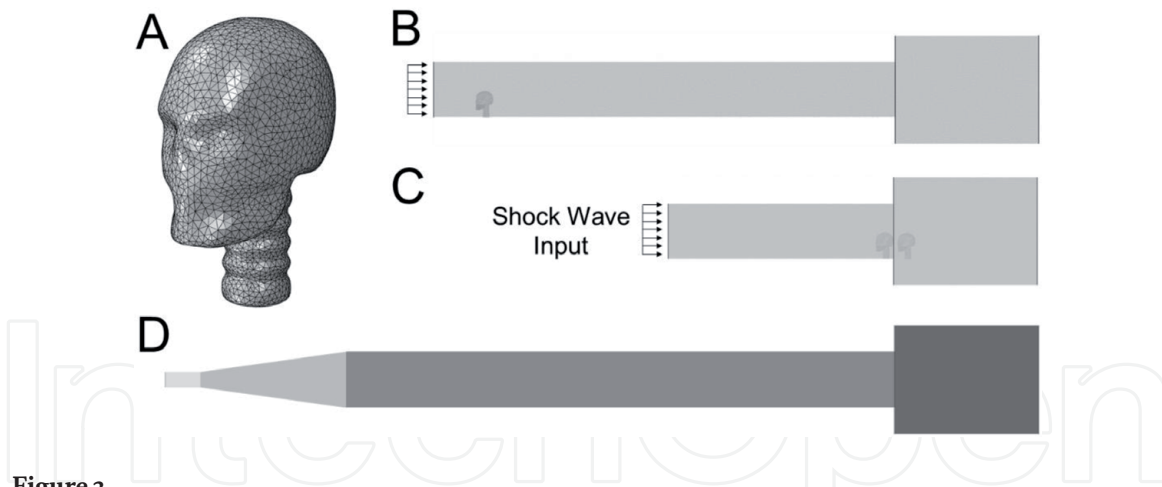


**Figure 3.**

The finite element models used in the calculation of the flow-fields around the headform. (A) The Lagrangian domain of the FOCUS headform was meshed using linear tetrahedral elements. The Eulerian domains were of two different lengths: (B) a 5.9 m length section downstream of the A2 sensor (Figure 1) to model the inside specimen location and (C) a 2.9 m length section downstream of the D5 sensor (Figure 1) to model the end and outside specimen locations. (D) The full shock tube size is shown, depicting the breech, expansion cone, driven region, and catch tank.

was assumed to be filled with air, approximated using the ideal gas equation of state at 296 K, a density of  $1.2 \text{ kg/m}^3$ , and a specific heat ratio of 1.4.

Twenty-seven simulated configurations were conducted, mirroring the experimental configurations of three specimen placement locations (inside, at the exit of, and outside the shock tube), three specimen orientations ( $0$ ,  $90$ , and  $180^\circ$ ), and three blast overpressures (70, 140, and 210 kPa). The shock was simulated as a planar pressure wave, applied to a surface upstream from the headform. For each configuration, pressure measurements taken at the sensor coincident with the loading surface were averaged for the four repeated exposures to create an input incident pressure pulse. The pressure pulse for a 210 kPa exposure with the headform located at the exit was used as the pressure pulse for the untested configuration of 210 kPa with the headform outside of the shock tube. All nodes coincident to the walls of the Eulerian domain and the base of the Lagrangian headform were constrained against all translational and rotational degrees of freedom. The enhanced immersed boundary method allowed for the Lagrangian mesh to occupy void regions within the Eulerian mesh, enabling the computation of the interfacial surface. Interaction between the two domains was defined as hard general contact in the direction normal to the interacting surfaces and a frictionless contact in the tangential direction.

All simulations were conducted in Abaqus 6.13-4 on two Intel Xeon 2.10 GHz processors (Dassault Systèmes). For each configuration, the pressure in each element along the vertical longitudinal plane was mapped to plot the blast overpressure (BOP), impulse, and rise time amplification factors (MATLAB R2019a, Mathworks). Element-wise values for the peak BOP were defined as the maximum simulated pressures, the impulses were calculated as the area under the pressure-time curves, and the rise times were calculated as the time required for the signal to increase from 10 to 90% of the peak value. Element-wise values were normalized with values of the incident waveform at that location, resulting in unitless amplification factors.

### 3. Results

#### 3.1 Experimental surface pressures on the headform

Representative pressure profiles recorded by the surface sensors mounted on the headform are presented in Figure 2B-D. These data were recorded at a nominal

shock wave intensity of 70 kPa, and general trends in pressure waveforms distribution are similar for the other two incident shock wave intensities (140 and 210 kPa). The effect of the headform rotation on the surface loading is illustrated in **Figure 2** for the inside test location. In general, on the face exposed to the shock wave the recorded peak overpressures are the highest: 245 kPa (H1 sensor) for the 0° orientation (**Figure 2B**, H8 and H9 sensors are a special case, considering the sensors are located in the concave “eye sockets” which results in the pressure entrapment, and extremely high peak overpressure values), 220 kPa (H7 sensor) for 90° orientation (**Figure 2C**, inset), and 225 kPa (H5 sensor) for 180° orientation (**Figure 2D**). It is obvious that the same trends are observed for the other two test locations and headform orientations (**Figure 4A–C**). It appears that the rise time is a sensitive metrics for the headform loading (**Figure 4D–F**). In general, the rise time is shortened on the front face exposed to the shock wave (H1 at 0° orientation, **Figure 4D**, H6 and H7 at 90° orientation, **Figure 4E**, and H5 at 180° orientation, **Figure 4F**) or it is extended on the converse side of the headform (H4 and H5 at 0° orientation in **Figure 4D**, H10 at 90° orientation in **Figure 4E**, and H1 and H2 at 180° orientation in **Figure 4F**), compared to the rise time of the incident shock wave. This effect is seen regardless of the headform test location. For the duration and impulse, a different kind of relationship is noticeable. It is expected considering both peak overpressure and the rise time are describing the behavior of the front face of the waveform, while the duration and the impulse are related to the properties of the entire waveform. In general, the duration and impulse values decrease with distance from the breach, corresponding with the test location in the order: inside > end > outside. This is associated with the erosion of the incident wave tail by the end effect. The shock wave exiting the shock tube creates a region of underpressure

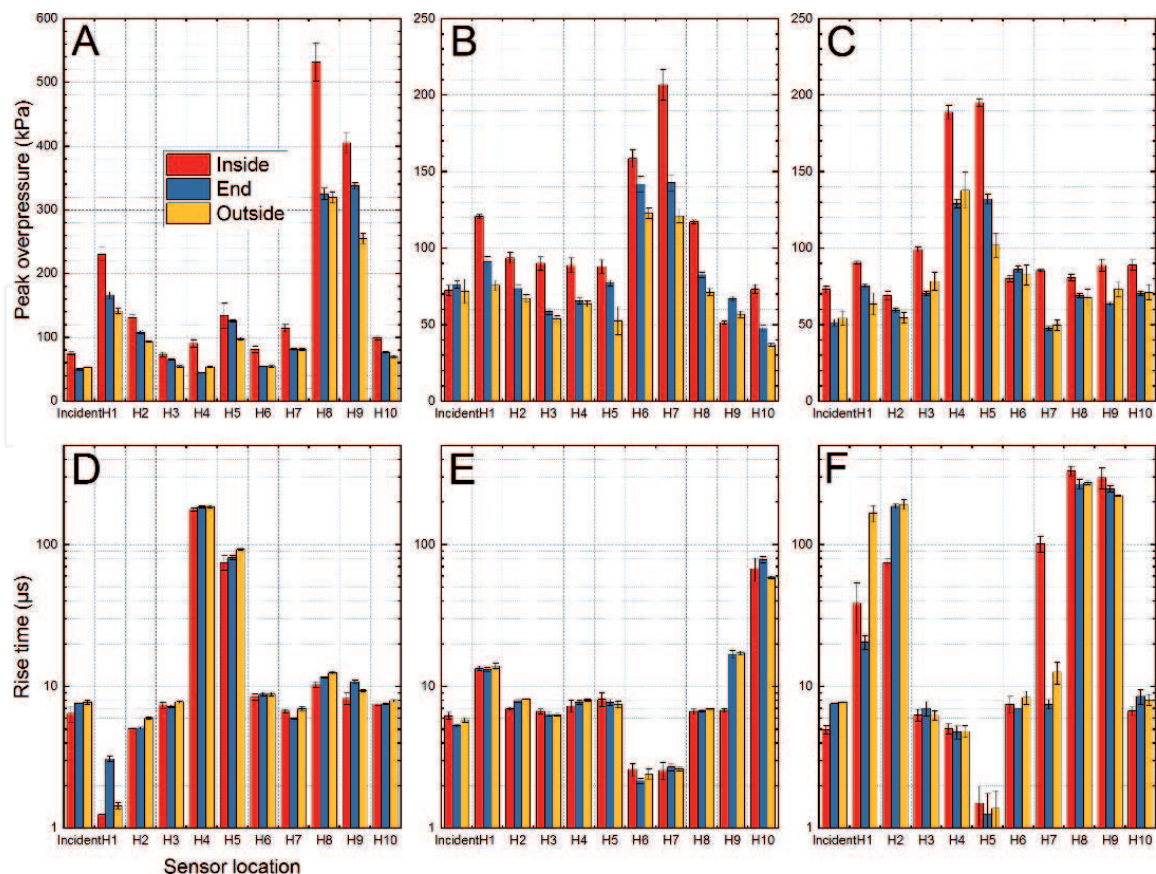


**Figure 4.** The results of the pressure waveforms characteristics quantification. The peak overpressure and the rise time for the incident and surface mount sensors collected at three different test locations (inside, end and outside) are presented (n = 4). The headform orientation in these experiments was 0° (A, C), 90° (B, E), and 180° (C, F).

which travels back into the shock tube [7], and unconfined conditions on the outside allow for free expansion of the previously constrained shock front, resulting in a conversion of the static pressure to ‘jet wind’, resulting in a shorter durations and lower impulse values at the end and outside locations (Figure 5).

### 3.2 Experimental data normalization

It is thus obvious a further data reduction is necessary in order to compare data collected at three different intensities and three different headform locations. The simplest and most natural approach is to take the characteristic parameters of the incident shock wave waveform (input) recorded by a sensor mounted at specific test location, i.e., T5 for inside, D7 for end and PP for outside location, and compare them with waveforms recorded by pressure sensors on the headform (output). The resulting dimensionless parameters (calculated using Eq. (1)) are a measure of the disturbance caused by introduction of headform into the flow field of the shock wave traveling in the shock tube. The values other than 1 indicate divergence from the waveform characteristics at specific test location in or outside of the shock tube and on the specific location on the headform, compared to the incident shock wave. These can be attributed to geometric factors, changes in shock wave characteristics and presence of additional high velocity flows which are below the detection levels of small cross section sensors sparsely distributed on the surface of the headform. However, if the shock wave properties were only gradually evolving while traveling in the shock tube, it is reasonable to expect similar distribution of non-dimensional parameters as a function of their physical location on the headform which becomes the only defining parameter of the system.

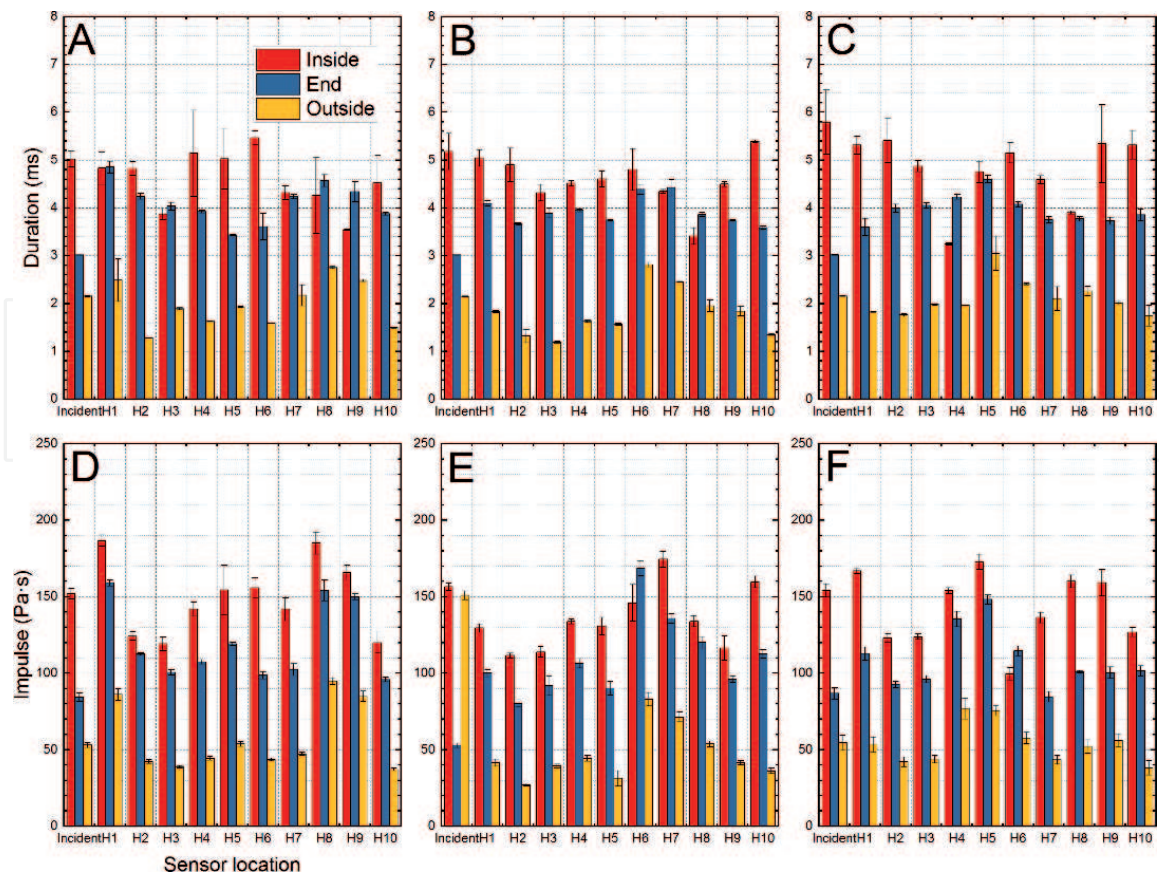


**Figure 5.** The results of the pressure waveforms characteristics quantification. The peak duration and the impulse for the incident and surface mount sensors collected at three different test locations (inside, end and outside) are presented ( $n = 4$ ). The headform orientation in these experiments was  $0^\circ$  (A, C),  $90^\circ$  (B, E), and  $180^\circ$  (D, F).

The non-dimensional parameters (or amplification factors) allow for direct comparison of pressure waveform characteristic parameters generated by a range of incident shock waves differing in intensity. Using this concept in mind we performed further data reduction for peak overpressures, rise time, impulse and durations in all datasets. The representative bar plot for the amplification factors for the peak overpressure, rise time, duration and impulse for the headform in the 90° orientation and exposed to a shock wave with three nominal intensities (70, 140 and 210 kPa) in three different locations (inside, end and outside) is presented in **Figure 6**. This figure illustrates that indeed the normalization is an effective strategy to compare the data obtained from a variety of exposure conditions. The normalized peak overpressure and rise time follow well defined trends, and the largest divergence is observed for the normalized duration and impulse at the end test location (**Figure 6C** and **D**). It is expected considering duration and impulse values for the end and outside locations vary more significantly than these reported by the headform sensors in the inside location (**Figure 5**).

We previously reported similar trends for the headform tested in the 0° orientation (see Figure 7 in Ref. [26]), and this work expands upon these results by incorporation of two additional orientations (90 and 180°). The data are presented as a function of the sensor distance of the 2D projection of the headform (for details refer to Figure 7B in Ref. [26]). The best results were noted for amplification factors of peak overpressure recorded on the headform at 0° orientation (**Figures 7, 8** and **Table 1**): the data collected in all three test locations has narrow distribution and follows well defined trend. Front sensor H1 has increased values in the range of 2.4–3.6, which gradually decrease along the headform reaching minimum values

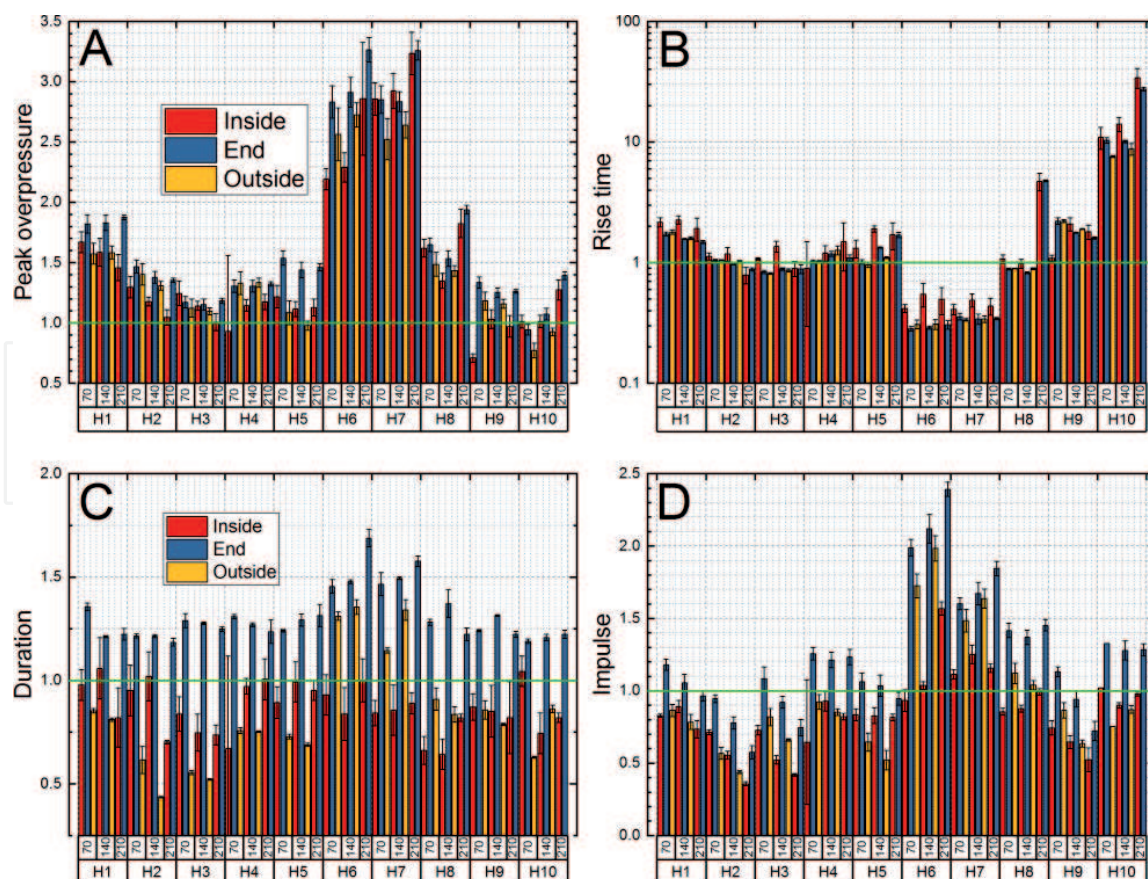


**Figure 6.** The results of the pressure waveform characteristics quantification for headform mounted sensors. The normalized peak overpressure (A), rise time (B), duration (C) and impulse (D) are presented ( $n = 4$ ) for experiments where the headform was mounted at 90° orientation. The normalization allows comparison of the data quantified for three nominal shock wave intensities: 70, 140 and 210 kPa.

of about 1 for the H4 and H6 sensors on the back of the headform, and reaching a value of 2 for the H5 sensor at the very end of the headform. This increase is purely due to combined effect of the shock wave wrapping around the headform and its two streams joining together at the back. This is accompanied by increased values for the rise time for H5 sensor by a factor of 10 compared to incident shock wave, which is markedly increased compared to all other sensors, where the rise time amplification factor never exceeds the value of 2 (Figure 7). Amplification factors for sensors mounted in the eye sockets are extremely high (in the range of 5–8),

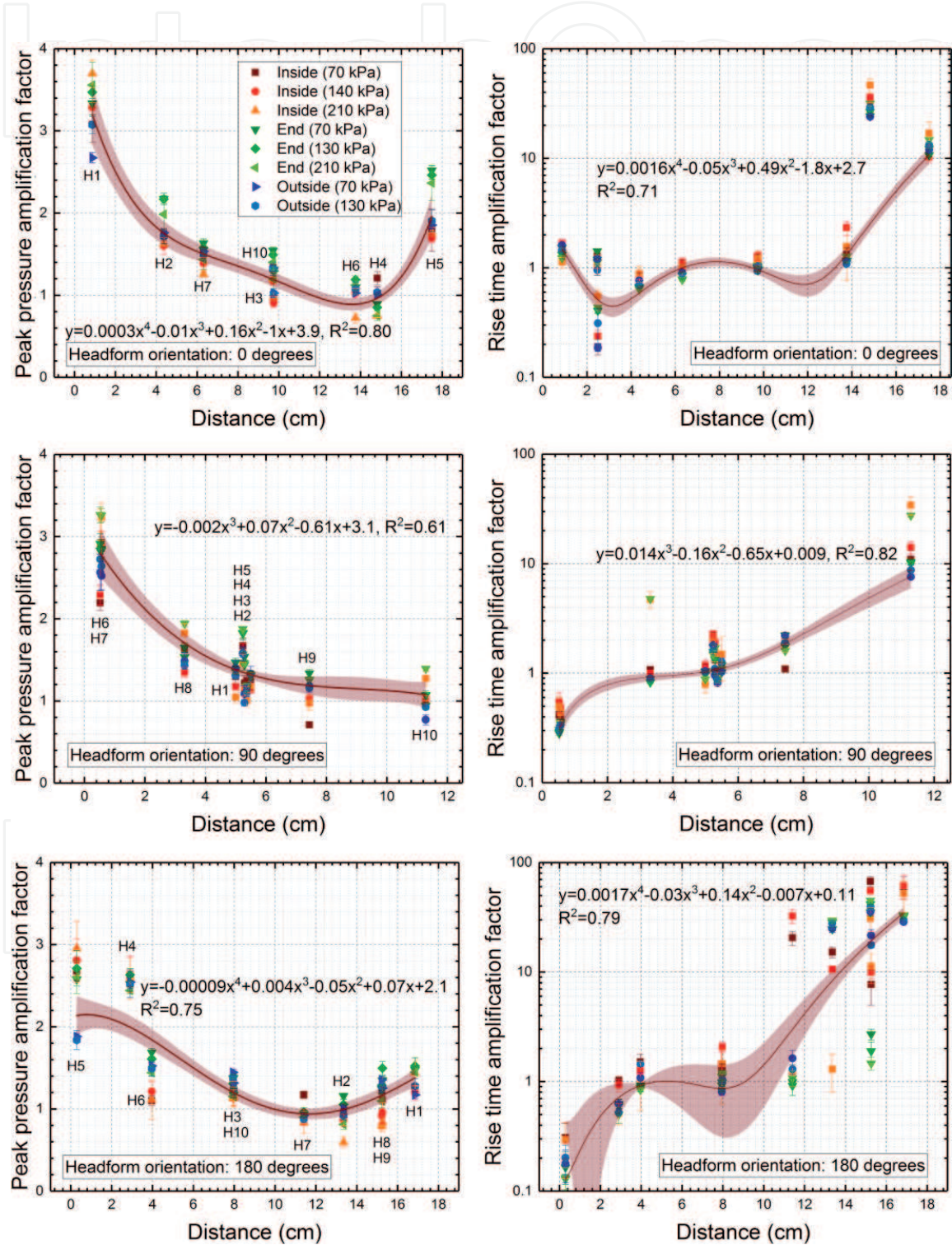


**Figure 7.** Amplification factors for peak overpressure and rise time as a function of the headform sensor distance. Polynomial fit performed on normalized data collected for three headform orientations of 0, 90 and 180° at three different test locations (inside, end and outside), three shock wave intensities (as indicated in the figure legend: 70, 140 and 210 kPa) and repeated four times. Adjusted  $R^2$  values vary from 0.82 (good fit) to 0.59 (mediocre fit) due to broad data distributions. Data are presented as average and standard deviation.

and they do not follow the same trend as sensors mounted on the flat surface of the headform. The concave geometry of eye sockets is responsible for the compressed air entrapment and momentary stagnation during shock wave exposure, which results in extreme pressures, compared to other locations on the headform. Similar trends are also noticeable for the 90 and 180° orientations, with differences related to the geometrical factors. The amplification factors on the face exposed to the shock wave (H6, H7 for the 90°, and H5 for 180° orientation) have lower values (<3) compared to 0° orientation. The rise time for these two orientations have much

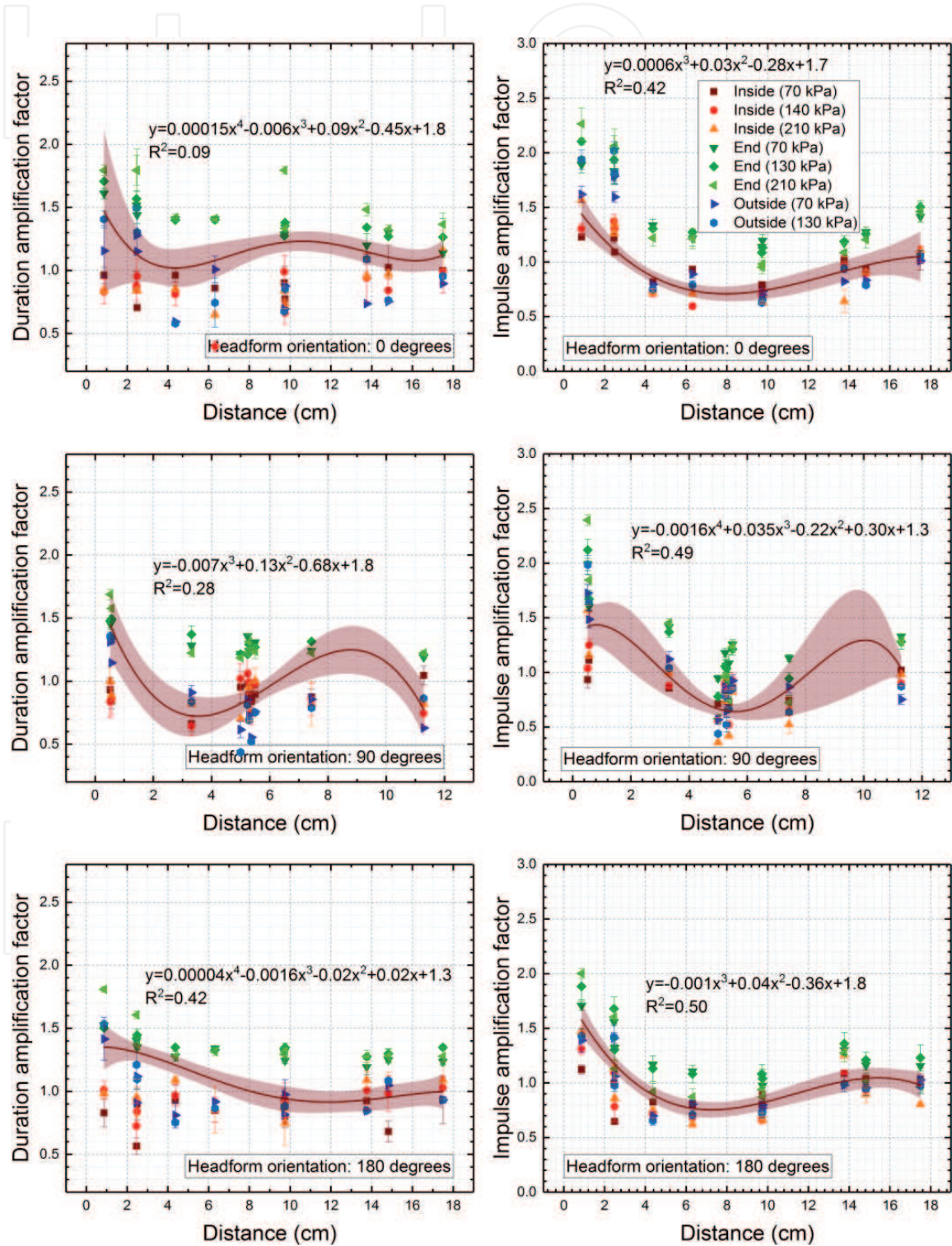


**Figure 8.** Amplification factors for the duration and impulse as a function of the sensor distance on the headform. Polynomial fit performed on normalized data collected for three headform orientations of 0, 90 and 180° at three different test locations (inside, end and outside), three shock wave intensities (as indicated in the figure legend: 70, 140 and 210 kPa) and repeated 4 times. Adjusted  $R^2$  values vary from 0.82 (good fit) to 0.04 (bad fit) due to broad data distributions. Data are presented as average and standard deviation.

lower values ( $<1 \mu\text{s}$ ) and rise time values gradually increase with increased distance (**Figure 7**). Far less consistent results are obtained for the duration and impulse values (**Figure 8**). The spread of amplification factor values in all six cases is 1.0 or more, which indicates that the loading conditions at specific test location plays an important role. These variations are expressed in the goodness of fit parameters (adjusted  $R^2$ ) which are presented in **Table 1**. It is clear fit parameters for peak overpressure and rise time indicate good fit, while for duration and impulse the parameters are below 0.5, which is indicative of poor-quality fit. The dispersion of the data points is the main reason, and respective data sets appear to follow stochastic distribution pattern rather than a single well-defined function.

### 3.3 Numerical simulation data normalization

The trends observed experimentally were confirmed using the numerical simulations. Normalized results for the spatial distribution of peak overpressures

Headform orientation	0°	90°	180°
Peak overpressure	0.80	0.61	0.75
Rise time	0.71	0.82 <sup>1</sup>	0.79 <sup>1</sup>
Impulse	0.42	0.49	0.50
Duration	0.09	0.28	0.42

<sup>1</sup>Large spread of the data for 90 and 180° orientations.

**Table 1.**

Adjusted  $R^2$  values for fits to different datasets presented in **Figures 6 and 7**.

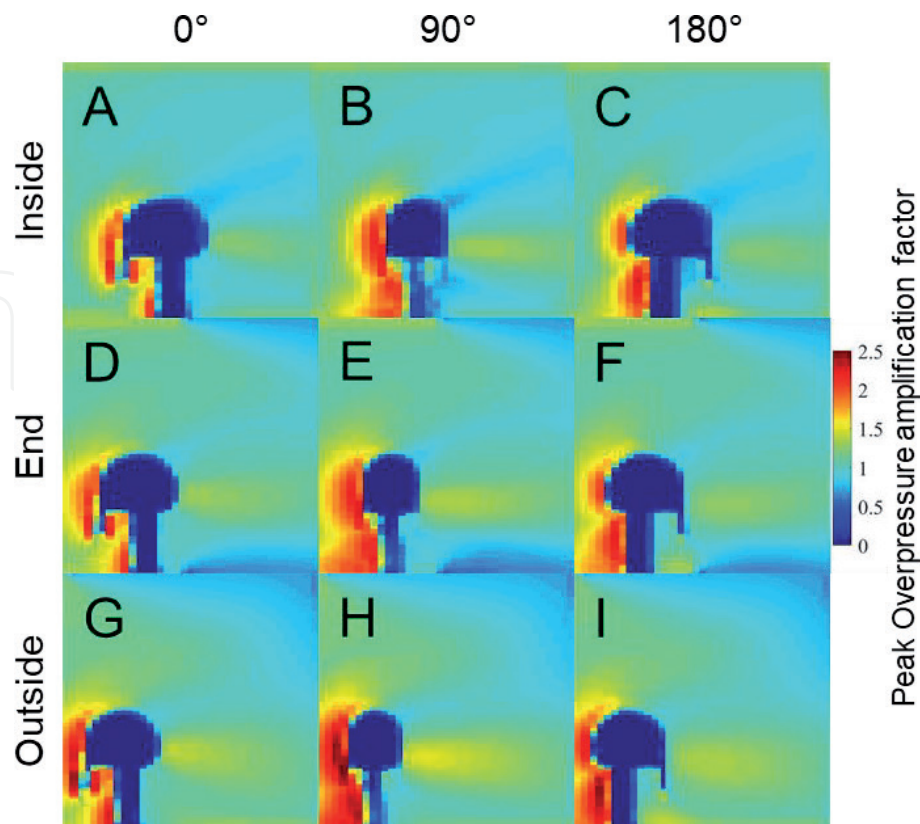


**Figure 9.**

Spatial distribution of the peak overpressure amplification factors for the 140 kPa exposures in the region surrounding the headform for three specimen locations and for three headform orientations.

confirmed that the highest peak overpressures are seen at the front face of the headform (**Figure 9**). Following data normalization, trends were found to be common between the three shock wave intensities, 70, 140, and 210 kPa, and, therefore, only results for 140 kPa exposures are shown. The area of stagnation is largest in the 90° orientation, followed by the 180° orientation. Additionally, for similar headform orientations, the area of stagnation increased with increasing distance from the breech, with the largest area of stagnations observed in the outside test locations and the smallest area observed at the inside location. A region of increased peak overpressures is observed behind the headform, regardless of the headform orientation or the testing location. This region indicates the area affected after the shock front wraps around the headform. Above and below that area of elevated peak overpressures, the lowest pressures are observed. This phenomenon is most apparent in the inside test location (**Figure 9A–C**), as a fan radiating behind the headform. These results corroborate the observed trends reported in **Figure 7**. The rise time was highest around the posterior face of the headform in all headform orientations and underneath the chin of the headform in the 0° orientation (**Figure 10**). In the area around the headform, the rise time was higher than that of the incident waveform. These trends were observed regardless of specimen location.

Spatial maps of the impulse amplification factors highlight the importance of testing location on specimen loading (**Figure 11**). The end location exhibited the largest impulse amplification factors and the inside location exhibited the smallest. This finding corroborates the wide spread of impulse and duration values reported in **Figure 8**. Furthermore, the impulse was highest in the 90° headform orientation, followed by the 180° orientation. The spatial distribution of the increased impulse was similar among specimen orientations and testing locations, differing in magnitudes only. A region of high impulse is seen on the front face of the headform and a region of low impulse, lower than the impulse of the incident wave, is seen behind the headform.

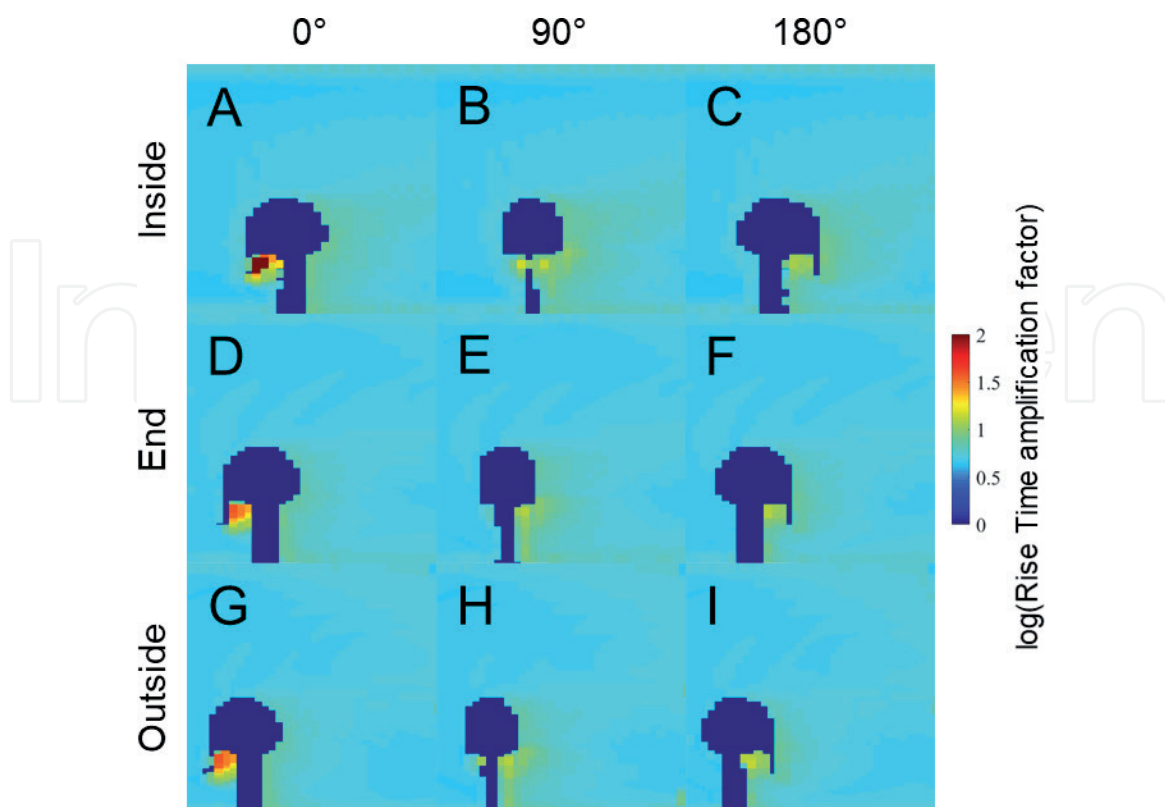


**Figure 10.** Spatial distribution of the rise time amplification factors for the 140 kPa exposures in the region surrounding the headform for three specimen locations and for three headform orientations. Data are reported as the log of the rise time amplification factor, indicated the order of magnitude of the change.

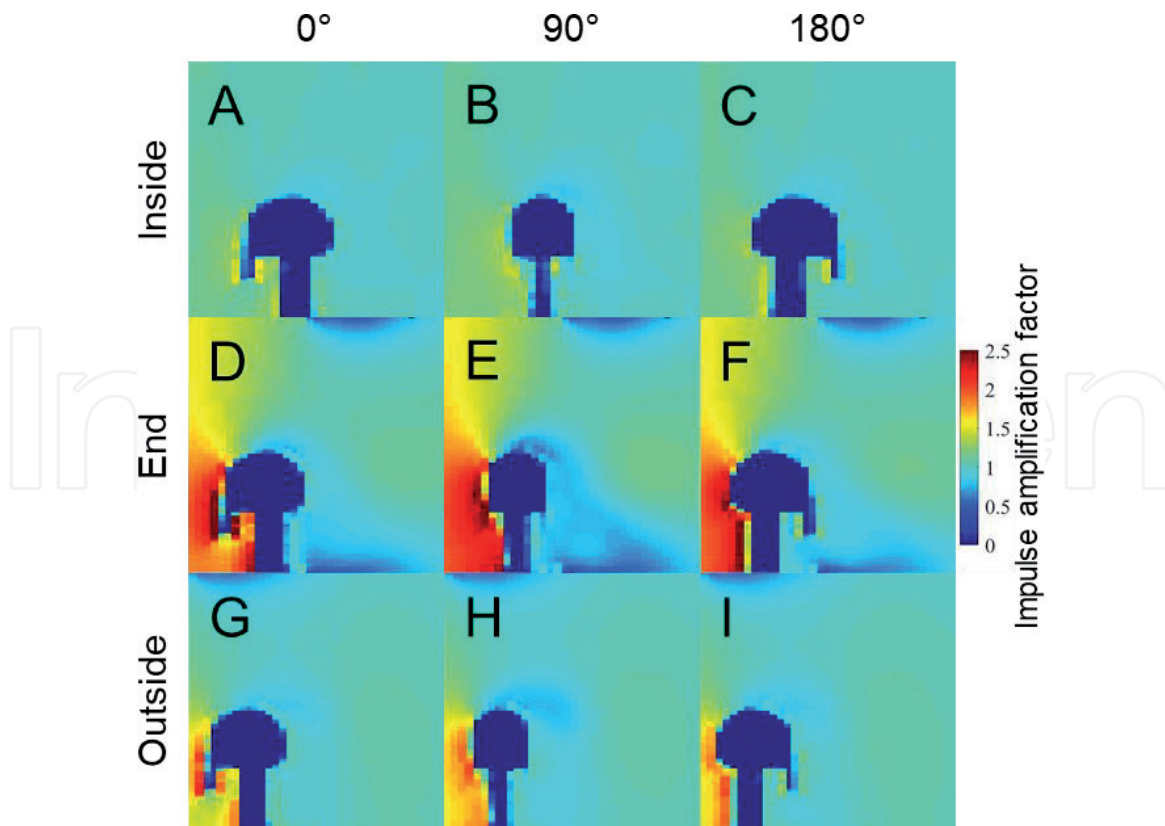


**Figure 11.**

*Spatial distribution of the impulse amplification factors for the 140 kPa exposures in the region surrounding the headform for three specimen locations and for three headform orientations. As the duration and impulse amplification factors showed similar results, only data for the impulse are presented here.*

#### 4. Conclusions

Headform instrumented with 10 pressure sensors (mounted to measure surface pressure) was exposed to a single shock wave with three nominal intensities: 70, 140, and 210 kPa. The headform was mounted in three different orientations: 0, 90 and 180° with respect to the direction of the shock wave propagation. The effect of the headform location was evaluated by positioning it inside of the shock tube, at the end and outside of the shock tube. The headform was mounted using Hybrid III biofidelic surrogate neck, which was tightened to eliminate the inertial motion of the headform caused by blast exposure.

Comparison of the test results at three different shock wave intensities complicates data analysis even further. To resolve these issues, we developed a simple strategy of data reduction: the respective pressure parameters recorded by headform sensors are divided by equivalent parameters of the incident shock wave as defined in Eq. (1). As a result, a comprehensive set of non-dimensional parameters is generated. These non-dimensional parameters (or amplification factors) allow for direct comparison of pressure waveform characteristic parameters generated by a range of incident shock waves differing in intensity and for the headform located in different locations.

Using this approach, we found there is a correlation function which allows prediction of the peak pressure on the headform which depends only on the peak pressure of the incident shock wave (for specific sensor location on the headform), and it's independent on the headform location, and to a certain degree the orientation. Similar relationship exists also for the rise time. However, for the duration and impulse similar correlation functions do not exist.

We demonstrated via comprehensive experimental and numerical studies that three different testing locations are characterized by non-equivalent loading

conditions. While it was possible to devise the transfer function for normalized peak overpressure and rise time at 0° orientation, the dispersion and clustering of data points indicates the surface pressure distribution is a function of the headform orientation where geometrical factors play important role.

## **Acknowledgements**

This work was supported by PEO Soldier award no. W91CRB-16-C-0025.

## **Conflict of interest**

The authors declare no conflict of interest.

## **Author details**

Maciej Skotak, Molly T. Townsend, Eren Alay and Namas Chandra\*  
Department of Biomedical Engineering, Center for Injury Biomechanics, Materials,  
and Medicine, New Jersey Institute of Technology, Newark, NJ, USA

\*Address all correspondence to: [namas.chandra@njit.edu](mailto:namas.chandra@njit.edu)

## **IntechOpen**

© 2019 The Author(s). Licensee IntechOpen. This chapter is distributed under the terms of the Creative Commons Attribution License (<http://creativecommons.org/licenses/by/3.0>), which permits unrestricted use, distribution, and reproduction in any medium, provided the original work is properly cited. 

## References

- [1] Vieille P. Sur les discontinuités produites par la détente brusque de gaz comprimés. Comptes Rendus de l'Académie des Sciences. 1899; A 129:1228-1230
- [2] Celander H, Clemedson C-J, Ericsson UA, Hultman HI. The use of a compressed air operated shock tube for physiological blast research. Acta Physiologica Scandinavica. 1955;33(1):6-13
- [3] Dryer M, Merritt DL, Aronson PM. Interaction of a plasma cloud with the Earth's magnetosphere. Journal of Geophysical Research. 1967;72(11):2955-2962
- [4] Hooker WJ, Millikan RC. Shock-tube study of vibrational relaxation in carbon monoxide for the fundamental and first overtone. The Journal of Chemical Physics. 1963;38(1):214-220
- [5] Kiefer J, Mizerka L, Patel M, Wei H. A shock tube investigation of major pathways in the high-temperature pyrolysis of benzene. The Journal of Physical Chemistry. 1985;89(10):2013-2019
- [6] Park C, Appleton JP. Shock-tube measurements of soot oxidation rates. Combustion and Flame. 1973;20(3):369-379
- [7] Kuriakose M, Skotak M, Misistia A, Kahali S, Sundaramurthy A, Chandra N. Tailoring the blast exposure conditions in the shock tube for generating pure, primary shock waves: The end plate facilitates elimination of secondary loading of the specimen. PLoS One. 2016;11(9):e0161597
- [8] Ganpule S, Alai A, Plougonven E, Chandra N. Mechanics of blast loading on the head models in the study of traumatic brain injury using experimental and computational approaches. Biomechanics and Modeling in Mechanobiology. 2013;12(3):511-531
- [9] Sundaramurthy A, Chandra NA. Parametric approach to shape field-relevant blast wave profiles in compressed-gas-driven shock tube. Frontiers in Neurology. 2014;5(253)
- [10] Mejia-Alvarez R, Wilson B, Leftwich M, Martinez A, Prestridge K. Design of a fast diaphragmless shock tube driver. Shock Waves. 2015;25(6):635-650
- [11] Tranter RS, Giri BR. A diaphragmless shock tube for high temperature kinetic studies. The Review of Scientific Instruments. 2008;79(9):094103
- [12] Takano Y, Akamatsu T. A diaphragmless shock tube. Journal of Physics E: Scientific Instruments. 1984;17(8):644
- [13] Swietek B, Skotak M, Chandra N, Pfister BJ. Characterization of a controlled shock wave delivered by a pneumatic table-top gas driven shock tube. Review of Scientific Instruments. 2019;90:075116
- [14] Heufer K, Olivier H, Drumm S, Murrenhoff H, editors. A new fast acting valve for diaphragmless shock tubes. In: 28th International Symposium on Shock Waves. Manchester, UK: Springer; 2012
- [15] Downey M, Cloete T, Yates A. A rapid opening sleeve valve for a diaphragmless shock tube. Shock Waves. 2011;21(4):315-319
- [16] Gageik M, Weiss A, Klioutchnikov I, Olivier H, editors. A numerical investigation of the flow through a new fast acting valve for diaphragmless shock tubes. In: 29th International

Symposium on Shock Waves . Vol. 1.  
Madison, WI, USA: Springer; 2015

[17] Skotak M, Alay E, Chandra N. On the accurate determination of shock wave time-pressure profile in the experimental models of blast-induced neurotrauma. *Frontiers in Neurology*. 2018;**9**:52

[18] Cernak I, Savic VJ, Kotur J, Prokic V, Veljovic M, Grbovic D. Characterization of plasma magnesium concentration and oxidative stress following graded traumatic brain injury in humans. *Journal of Neurotrauma*. 2000;**17**(1):53-68

[19] Cernak I, Wang Z, Jiang J, Bian X, Savic J. Cognitive deficits following blast injury-induced neurotrauma: Possible involvement of nitric oxide. *Brain Injury*. 2001;**15**(7):593-612

[20] Kobeissy F, Mondello S, Tumer N, Toklu H, Whidden M, Kirichenko N, et al. Assessing neuro-systemic & behavioral components in the pathophysiology of blast-related brain injury. *Frontiers in Neurology*. 2013;**4**:186

[21] Chandra N, Sundaramurthy A, Gupta RK. Validation of laboratory animal and surrogate human models in primary blast injury studies. *Military Medicine*. 2017;**182**:105-113

[22] Goldstein LE, Fisher AM, Tagge CA, Zhang X-L, Velisek L, Sullivan JA, et al. Chronic traumatic encephalopathy in blast-exposed military veterans and a blast neurotrauma mouse model. *Science Translational Medicine*. 2012;**4**(134):134ra60-134ra60

[23] Gullotti DM, Beamer M, Panzer MB, Chia Chen Y, Patel TP, Yu A, et al. Significant head accelerations can influence immediate neurological impairments in a murine model of blast-induced traumatic brain injury. *Journal of Biomechanical Engineering*. 2014;**136**(9):091004-091011

[24] Alay E, Skotak M, Misistia A, Chandra N. Dynamic loads on human and animal surrogates at different test locations in compressed-gas-driven shock tubes. *Shock Waves*. 2017;**28**(1):51-62

[25] Sundaramurthy A, Alai A, Ganpule S, Holmberg A, Plougonven E, Chandra N. Blast-induced biomechanical loading of the rat: An experimental and anatomically accurate computational blast injury model. *Journal of Neurotrauma*. 2012;**29**(13):2352-2364

[26] Skotak M, Alay E, Zheng JQ, Halls V, Chandra N. Effective testing of personal protective equipment in blast loading conditions in shock tube: Comparison of three different testing locations. *PLoS One*. 2018;**13**(6):e0198968

[27] Needham CE, Ritzel D, Rule GT, Wiri S, Young L. Blast testing issues and TBI: Experimental models that lead to wrong conclusions. *Frontiers in Neurology*. 2015;**6**:72

[28] Abate G, Shyy W. Dynamic structure of confined shocks undergoing sudden expansion. *Progress in Aerospace Sciences*. 2002;**38**(1):23-42

[29] Arakeri J, Das D, Krothapalli A, Lourenco L. Vortex ring formation at the open end of a shock tube: A particle image velocimetry study. *Physics of Fluids*. 2004;**16**(4):1008-1019

[30] Moore DF, Jérusalem A, Nyein M, Noels L, Jaffee MS, Radovitzky RA. Computational biology—Modeling of primary blast effects on the central nervous system. *NeuroImage*. 2009;**47**:T10-T20

[31] Roberts J, Harrigan T, Ward E, Taylor T, Annett M, Merkle A. Human head-neck computational model for assessing blast injury. *Journal of Biomechanics*. 2012;**45**(16):2899-2906

- [32] Grujicic M, Bell WC, Pandurangan B, Glomski PS. Fluid/structure interaction computational investigation of blast-wave mitigation efficacy of the advanced combat helmet. *Journal of Materials Engineering and Performance*. 2010;**20**(6):877-893
- [33] Grujicic M, Bell WC, Pandurangan B, He T. Blast-wave impact-mitigation capability of polyurea when used as helmet suspension-pad material. *Materials & Design*. 2010;**31**(9):4050-4065
- [34] Merkle AC, Wing ID, Roberts JC. Human surrogate head response to dynamic overpressure loading in protected and unprotected conditions. In: Herold KE, Vossoughi J, Bentley WE, editors. 26th Southern Biomedical Engineering Conference SBEC 2010, April 30–May 2, 2010, College Park, Maryland, USA. Berlin, Heidelberg: Springer; 2010. pp. 22-25
- [35] Ganpule S, Gu L, Alai A, Chandra N. Role of helmet in the mechanics of shock wave propagation under blast loading conditions. *Computer Methods in Biomechanics and Biomedical Engineering*. 2012;**15**(11):1233-1244
- [36] Nyein MK, Jason AM, Yu L, Pita CM, Joannopoulos JD, Moore DF, et al. In silico investigation of intracranial blast mitigation with relevance to military traumatic brain injury. *Proceedings of the National Academy of Sciences*. 2010;**107**(48):20703-20708
- [37] Ott K, Voo L, Merkle A, Iwaskiw A, Wickwire A, Wester B, et al. Experimental determination of pressure wave transmission to the brain during head-neck blast tests. In: *Proceedings of the ASME 2013 Summer Bioengineering Conference* 26-29 June 2013. Sunriver, Oregon, USA. 2013;**55607**:V01AT10A006. DOI: 10.1115/SBC2013-14834
- [38] Zhang L, Makwana R, Sharma S. Brain response to primary blast wave using validated finite element models of human head and advanced combat helmet. *Frontiers in Neurology*. 2013;**4**:80
- [39] Przekwas A, Tan XG, Harrand V, Reeves D, Chen ZJ, S K, et al. Integrated experimental and computational framework for the development and validation of blast wave brain biomechanics and helmet protection. In: *Proc HFM-207 NATO Symposium on a Survey of Blast Injury Across the Full Landscape of Military Science*; Oct. 3-5, 2011; Halifax NS, Canada. 2011. pp. 34-1-34-20
- [40] Grujicic M, Ramaswami S, Snipes J, Dudt P. Potential improvement in helmet blast-protection via the use of a polyurea external coating: Combined experimental/computational analyses. *Proceedings of the Institution of Mechanical Engineers, Part L: Journal of Materials: Design and Applications*. 2016. DOI: 10.1177/1464420716644472
- [41] Ouellet S, Bir C, Bouamoul A. Direct Comparison of the Primary Blast Response of a Physical Head Model with Post-Mortem Human Subjects. QC Canada: Defence Research and Development Canada-Valcartier Research Center Quebec; 2014
- [42] Ganpule S, Salzar R, Perry B, Chandra N. Role of helmets in blast mitigation: Insights from experiments on PMHS surrogate. *International Journal of Experimental and Computational Biomechanics*. 2016;**4**(1):13-31
- [43] Zhu F, Wagner C, Dal Cengio Leonardi A, Jin X, VandeVord P, Chou C, et al. Using a gel/plastic surrogate to study the biomechanical response of the head under air shock loading: A combined experimental and

numerical investigation. *Biomechanics and Modeling in Mechanobiology*. 2012;**11**(3):341-353

[44] Banton R, Piehler T, Zander N, Benjamin R, Duckworth J. Comparison of numerical simulations with experiments of blast-induced pressure wave impact on a surrogate head model. In: Kimberley J, Lamberson L, Mates S, editors. *Proceedings of the 2017 Annual Conference on Experimental and Applied Mechanics, Dynamic Behavior of Materials*. Vol. 1. Cham: Springer International Publishing; 2018. pp. 181-187

[45] Crowley JS, Brozoski FT, Duma SM, Kennedy EA. Development of the facial and ocular countermeasures safety (FOCUS) headform. *Aviation, Space, and Environmental Medicine*. 2009;**80**(9):831

[46] Foster JK, Kortge JO, Wolanin MJ. Hybrid III-A biomechanically-based crash test dummy. SAE International. 1977. p. 770938. DOI: 10.4271/770938

[47] Mougeotte C, Carlucci P, Recchia S, Ji H. Novel approach to conducting blast load analyses using Abaqus/explicit-CEL. In: Center AARDE, editor. *Picatinny Arsenal*. NJ: Defense Technical Information Center; 2010

[48] Tan XG, Przekwas AJ, Gupta RK. Computational modeling of blast wave interaction with a human body and assessment of traumatic brain injury. *Shock Waves*. 2017;**27**(6):889-904

[49] Townsend MT, Alay E, Skotak M, Chandra N. Effect of tissue material properties in blast loading: Coupled experimentation and finite element simulation. *Annals of Biomedical Engineering*. 2018:1-14. DOI: 10.1007/s10439-018-02178-w